Morphology and evolution of cold-frontal misocyclones

D. J. Smart[a]* and K. A. Browning[b]

[a]*Independent Researcher, London, UK*
[b]*Independent Researcher, Ambleside, UK*

ABSTRACT: A numerical simulation of an intense, narrow cold-frontal rain band (NCFR) is presented. This front was associated with localized wind damage as it moved eastwards across the United Kingdom on 24 September 2007. The model used was the operational and research Weather Research and Forecasting–Advanced Research (WRF–ARW) mesoscale model, initialized with Global Forecast System (GFS) operational model output data. The simulation produced a front strongly resembling that seen in radar imagery and conforming to previous studies and conceptual models of the ana-cold front. In the simulation, a strong surface horizontal wind-speed maximum is located along the southern flank of a misocyclone; this is shown to be typical of a number that form along the front. Using trajectory analysis, descending cold air parcels, which originate in the rear inflow jet and accelerate within the circulation of the misocyclone, are identified as the origin of the strongest winds. In addition to the localized strong straight-line winds, circumstantial evidence is presented for the possible occurrence of weak tornadogenesis. The results are discussed in relation to recent studies of NCFRs, squall lines and misocyclones. Copyright © 2009 Royal Meteorological Society

1. Introduction

Narrow swathes of minor wind damage commonly occur in the UK in association with the passage of intense cold fronts. The kind of cold front responsible for such events is the ana-cold front as classified by Sansom (1952). Bradbury and Deaves (1994), in a statistical study, identified a population of extreme wind gusts associated with convection and convective ana-cold fronts. Bradbury *et al.* (1994) emphasized the importance of such extreme gusts to designers and operators of wind-sensitive infrastructure as well as operational weather forecasters.

Ana-cold fronts are characterized near the surface by a sharp frontal transition zone. The cold air behind the surface cold front (SCF) behaves rather like a density current, at the leading edge of which there is usually a line of shallow but relatively strong updraughts and heavy precipitation. Browning and Harrold (1970) in an early Doppler radar study referred to this as 'line convection'. A feature of line convection first emphasized by James and Browning (1979) and Hobbs and Biswas (1979) is that the intense precipitation occurs in segments or cores separated by discontinuities or gaps of weaker rainfall, which can be detected by operational weather radars. Other studies confirmed the nature of line convection and attributed the observed core/gap morphology to the presence of horizontal shearing instability (Haurwitz, 1949), hereafter 'HSI', (Houze *et al.*, 1976; Matejka *et al.*, 1980; Hobbs and Persson, 1982; Carbone 1982, 1983).

The horizontal shear at the SCF is of the order of 0.01 s^{-1} and this gives rise to a quasi-two-dimensional sheet of vertical vorticity that rolls up to form small vortices. Vortical circulations of this type, with horizontal dimensions of the order of 1 km and wind field dimensions in the range 40–4000 m, were termed 'misocyclones' by Fujita (1981). Lee and Wilhelmson (1997a) carried out idealized modelling of this process for thunderstorm outflows.

Narrow cold-frontal rain bands (NCFRs) propagate into an environment of weak instability or neutral stability and are not to be confused with a different class of phenomenon found when thunderstorm outflows propagate into a pre-frontal environment with convective available potential energy (CAPE) in excess of ∼ 1000 J kg^{-1}, the so-called 'bow echo' mesoscale convective system or quasi-linear convective system (QLCS) (see Wakimoto, 2001, for a review).

Recent studies of cold-season NCFRs, as well as QLCSs, using operational radar imagery in the United States have identified a radar signature, the 'broken-S', that is related to the segmented structure referred to above. This is associated with the presence of HSI, the line-echo wave pattern (LEWP) (Nolen, 1959) and also the occurrence of mesocyclone-like circulations, tornadoes and severe wind damage (McAvoy *et al.*, 2000; Grumm, 2004). Lane and Moore (2006) emphasize the challenge to forecasters posed by such phenomena. Tornadic circulations may develop and dissipate within very brief periods of time – as little as one interval between operational radar scans (∼5 min). Moreover, rotation is confined within the lowest few thousand feet

*Correspondence to: D. J. Smart, 137 Ardgowan Road, London, SE6 1UY, UK. E-mail: david.smrt@gmail.com

above the ground and tornadogenesis occurs without the presence of a deep, persistent mesocyclone. Doppler radar observations and studies of tornadoes along NCFRs are relatively rare. A key case study is that of Carbone (1982, 1983) in which observations by multiple Doppler radars were synthesized to portray the parent circulation of a tornado on an intense cold front with gravity-current-like characteristics. Kobayashi *et al.* (2007) reported radar observations of a tornado along a cold-frontal rain band with core/gap structure in Japan. They found that the parent misocyclone had a diameter of 2 km and vorticity of the order of 10^{-2} s^{-1}.

In this article we present results from a very high-resolution numerical weather prediction (NWP) model, which describes the structure and evolution of a mildly damaging – and in that sense, probably quite typical – cold-frontal misocyclone in the UK. Our purpose will be to clarify the extent, duration and evolution of the small area of strong straight-line surface winds associated with the misocyclone and to identify the (recent) origin of the air parcels that gave the peak gusts at the surface. Five misocyclones are identified, from a number of simulations, and their properties compared. Circumstantial evidence is presented for the possible occurrence of brief tornadogenesis early in the lifecycle of one misocyclone.

In section 2 the numerical model and its configuration are briefly described, and the results assessed in relation to available observations. In section 3.1 an overview of the synoptic context and frontal structure on the meso-scale is given. One misocyclone, considered typical, is examined in detail in sections 3.2 and 3.3. The properties of this misocyclone and four others are compared in general in section 3.4. In section 4 the present case study is discussed and related to previous studies mentioned above. Conclusions are presented in section 5.

2. Description of the numerical model and overview of results

The simulations in this article were conducted with the Weather Research and Forecasting–Advanced Research (WRF–ARW) model version 2.1.2 (Skamarock *et al.*, 2005). The non-hydrostatic Advanced Research WRF (ARW) dynamical core was used in a nested grid configuration. The outer nest, or 'mother domain', covered a large area of the UK at 13.5 km grid point spacing; further nests, domains d02, d03, d04, were centred on the region of interest at 4.5, 1.5 and 0.5 km grid point spacing respectively (Figure 1(a)). The grid point spacing of 500 m on the innermost domain was considered sufficient to resolve the phenomena we are interested in – vorticity maxima with diameters of < 4 km – as they were robust features in our simulations with grid point spacing of 2 km or less and in simulations reported in the literature (Trapp and Weisman, 2003; Wheatley and Trapp, 2008). The very high-resolution domain d04 consisted of 202 × 148 grid points (101 × 74 km) in the horizontal plane. The locations of the model nests for a typical simulation are shown in Figure 1. There were 48 levels in the vertical with the first level above the model surface terrain at 24 m and final level at 2007 m below the model top at 50 hPa. Open boundary conditions were applied at the model top. No spurious waves were detected due to reflection from the upper boundary. The model levels were concentrated in the lower part of the troposphere with 30 levels below 600 hPa. Test runs with 60 and 90 levels indicated that 48 levels were sufficient to resolve the structure of the rain band and little would be gained by increasing the vertical resolution, although increased maximum vertical relative vorticity (hereafter 'vertical vorticity') values of ∼10–20% were noted for the 90 level test run. A 2 or 3 second time step was used on the 500 m domain.

Physics options used were the Lin *et al.* microphysics scheme (Lin *et al.*, 1983), including graupel, on all four domains and the Kain–Fritsch cumulus
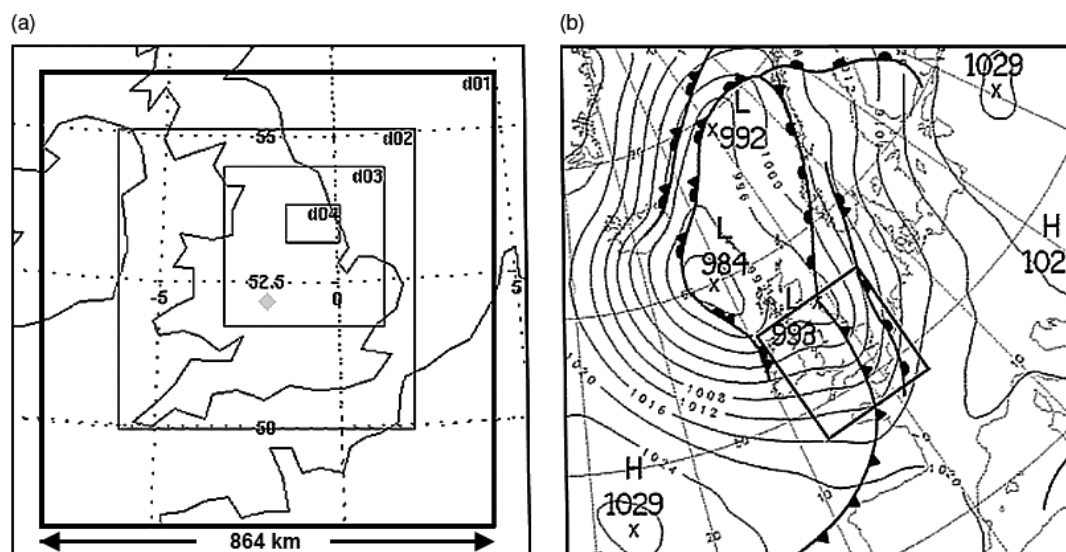

Figure 1. Synoptic overview and location of model nested domains. (a) Location of the model domains, d01–d04. (b) Section of UK Meteorological Office surface analysis at 0600 UTC on 24 September 2007 (courtesy and copyright UKMO). The area of model domain d01 is outlined.

parametrization scheme (Kain, 2004) on the 13.5 km resolution mother domain only. Cumulus convection was represented explicitly on the inner domains. The Noah land surface model (Chen and Dudhia, 2001), Yonsei State University (YSU) planetary boundary layer scheme (Noh *et al.*, 2003), Rapid Radiative Transfer Model (RRTM) long-wave radiation (Mlawer *et al.*, 1997) and Dudhia shortwave radiation schemes (Dudhia, 1989) were used.

Initial and boundary conditions were obtained from the National Centers for Environmental Prediction (NCEP) Global Forecast System (GFS) model output at 0.5° resolution and updated every 3 hours. The 0000 UTC run on 24 September 2007 was used. The outer mother domain and domain d02 were run from 0000 UTC to 0900 UTC. Domain d03 was initialized at 0300 UTC and domain d04 at 0400 UTC and they were run until 0700 UTC. 'Spin up' times on the innermost grids were minimal, no practical difference was found by initializing at earlier times in test runs. History files of model output were saved every one minute for domain d04.

Initial simulations, with two-way interactive nesting, produced a rain band with excellent timing and locations compared with radar imagery but were marred by the presence of a stationary, intense precipitation feature apparently tied to model terrain topography. Controlled experiments did not isolate one single cause for this spurious feature. As we are primarily interested here in the results of the effects of large-scale, synoptic forcing on the mesoscale, the present simulation utilized one-way nesting and low-resolution terrain data interpolated from the 13.5 km 'mother' domain, thus eliminating the spurious rain band. The geographical terrain where this inner grid is located is of low altitude, less than ~100 m, and is not thought to influence the frontal structure significantly. The simulation produced a similar, realistic-looking cold-front rain band, but this now occurred 15–30 minutes too early compared with radar imagery. This difference in timing should be borne in mind when reading later discussions.

3. Case study of a misocyclone

3.1. Synoptic overview and structure of the cold front

On the morning of 24 September 2007 an intense cold front moved rapidly eastwards across the southern and central parts of the United Kingdom. The front was accompanied by a short period of intense rainfall, marked wind veer, an abrupt pressure jump and strong wind gusts. A gust of 67 mph ($\sim$30 m s^{-1}) was reported at Cranwell, Lincolnshire at 0700 UTC. On the passage of the front over the meteorological observatory at Chilbolton, Hampshire in southern England at around 0545 UTC automatic instrumentation recorded a pressure rise of 2–3 hPa, a drop in temperature and dew point of $\sim$5 °C, a sharp peak in rainfall intensity of 60 mm h^{-1} and a gust in wind speed in excess of 30 m s^{-1} as the wind direction veered from 200°–300° from north (http://www.chilbolton.rl.ac.uk/weather/metdata.htm, web page accessed 24 September 2007).

There were widespread reports of trees uprooted and localized damage to property from across central and eastern areas of the UK. The European Severe Weather Database (http://essl.org/ESWD/, web page accessed 13 November 2008) records six severe weather events for this day. All are classified anecdotally as tornadic in nature with intensity of F0 or F1 on the Fujita scale (Fujita, 1981), i.e. wind speeds were in the range $\sim$18–49 m s^{-1}. In addition on-line news sources (http://news.bbc.co.uk) also reported that damage occurred at Scunthorpe, Humberside at around 0620 UTC with trees blown over and damage to house roofs, suggesting the event was of intensity F0. There were also reports of damage from north of the River Humber. These locations appear close to an evolving gap feature seen in radar imagery and the path of a misocyclone (V1) in the simulation. Lack of systematic damage surveys precludes us from drawing further conclusions about the nature of the events, i.e. whether they were due to weak tornadoes or localized straight-line winds. Anecdotal reports suggest the damage tracks were of the order of a few tens of metres in width and a few hundreds of metres in length.

A section of the United Kingdom Meteorological Office (UKMO) 0600 UTC surface analysis chart on 24 September is shown in Figure 1(b). A complex area of low pressure was lying from the UK to the Norwegian Sea. Along a trailing cold front there was a frontal wave with its inflection point located just off the north-east coast of England. South of this feature intense cold frontogenesis was under way. Upper air charts (not shown) exhibit a jet streak, located from northern England to Norway, with winds in excess of 70 m s^{-1} at 300 hPa. This was associated with a short-wave feature propagating north-eastwards around the base of a trough at 500 hPa. Satellite water-vapour imagery (not shown) displays a large area of dry intrusion to the west of a sharply demarcated S-shaped cloud shield over eastern/north-eastern England and the northern North Sea indicative of baroclinic cyclogenesis. The surface cold front (SCF) was beneath this cloud shield and moved rapidly eastwards at approximately 11 m s^{-1}. The frontal wave feature subsequently developed into a low-pressure system, with a central pressure of 970 hPa, off Norway at 0000 UTC on 25 September.

Network radar imagery (not shown) displayed an intense SCF lying from north-eastern England to north-western France. The pattern of line convection along the front resembled that seen in previous studies of NCFRs (e.g. James and Browning, 1979). Examination of model fields (not shown) indicated there was strong flow in the lower troposphere in the warm air ahead of the SCF with a low-level jet reaching speeds of 30 m s^{-1} at 850 hPa. Such strong winds were not manifested at the surface generally, only locally along the SCF, and, as we shall show, were associated more with the cold air behind the front than with the warm air of the low-level jet. This jet peeled away from the boundary layer and flowed up and over the frontal head in a quasi-two-dimensional, slab-like fashion as previously described for some NCFRs (cf. Browning and Roberts, 1996). The

model pre-frontal environment was only weakly unstable with surface-based CAPE of no more than 240 J kg^{-1}. Model-diagnosed bulk shear from 0–2.5 km above the surface was of the order of 15 m s^{-1} along the SCF at 0500 UTC.

In Figure 2 we compare low-resolution radar imagery with simulated model radar reflectivity fields from the intermediate model domain d03. The network radar imagery shows a narrow band of intense precipitation, embedded in lighter precipitation, moving eastwards with time. There are numerous regions where the rain band intensifies and bows forward, interspersed with 'gaps' or regions of weaker echoes. The simulated radar reflectivity field from the intermediate domain, d03, mimics this evolution and morphology. In Figure 3(a) we show the evolution of the vertical vorticity field from domain d03. The vertical vorticity field evolved from a linear, two-dimensional structure into a series of discrete vorticity maxima. The evolution of vertical vorticity and near-surface horizontal wind-speed fields from the high-resolution domain d04 are shown in Figure 3(b). Regions of high horizontal wind speed,
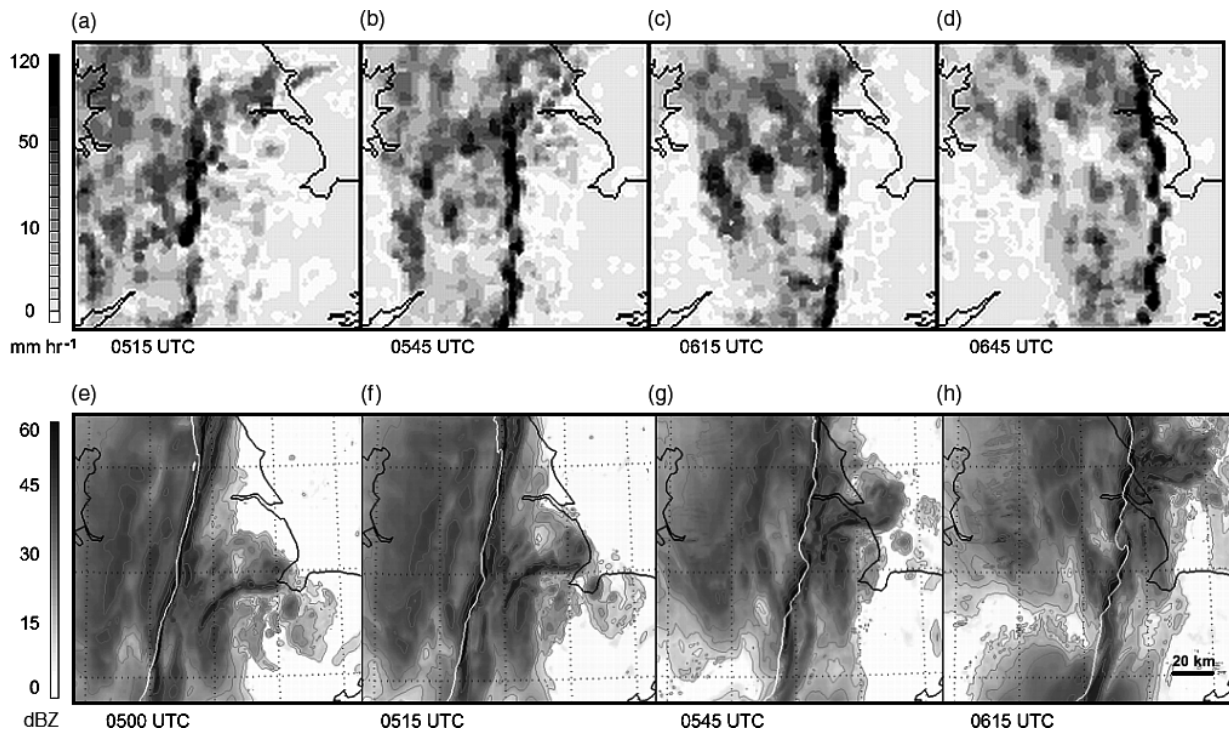

Figure 2. Comparison of low-resolution network radar imagery with model precipitation fields. (a)–(d) Network radar images (courtesy and copyright UKMO and Netweather UK), 0515 UTC–0645 UTC, 24 September 2007. (e)–(h) Model simulated composite radar reflectivity (dBZ), domain d03, 0500 UTC–0615 UTC. In order to show the approximate position of the surface cold front the 314 K θ_e contour at the 975 hPa level is plotted as a bold white line. Times of the radar imagery have been selected so that the frontal positions are approximately comparable with the times of model output. As noted in the text there is a 15–30 minute phase difference between the simulated and observed rain band.
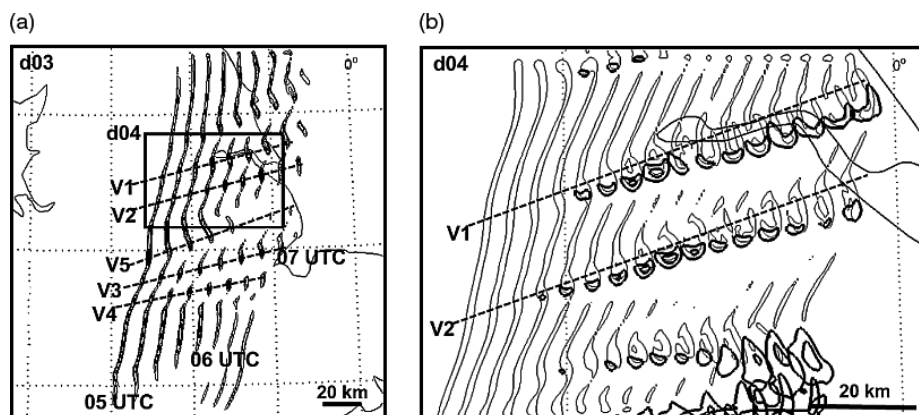

Figure 3. Evolution of model vertical vorticity and wind-speed fields. (a) Domain d03, vertical vorticity (s^{-1}) at 925 hPa, from 0500–0700 UTC, every 15 minutes, contour at 0.005 s^{-1}. Dashed lines indicate the approximate tracks of misocyclones V1–V5 (see section 3.4) . The area of domain d04 is outlined. (b) Domain d04, vertical vorticity (s^{-1}) at 925 hPa, from 0510–0625 UTC, every 5 minutes, light contours every 0.01 s^{-1}, starting at 0.01 s^{-1} .Wind speed (m s^{-1}) at 975 hPa, bold contours every 5 m s^{-1} from 25 m s^{-1}. Dashed lines indicate the approximate tracks of misocyclones V1 and V2. The fields near the northern and southern boundaries are distorted by interaction with the computational domain wall (see text).

>25 m s^{-1}, developed at or close to the surface along the southern flanks of the vorticity maxima. Figure 4(a) and (b) compare higher resolution radar imagery with the simulated radar reflectivity field from domain d03. The 500 m grid domain d04 is shown in Figure 4(c). The SCF is a narrow transition region of strong wind shear and veer. Perturbations along the front are clearly associated with vorticity maxima with a diameter of $\sim$4 km, i.e. 'misocyclones' (Fujita, 1981), and distortions of the frontal zone, here defined by the 314 K θ_e (equivalent potential temperature) contour, where the leading edge bows forward. The simulated rain band and radar 'line convection' possess common features, i.e. a well-defined leading edge with areas of intense precipitation, a rearward trailing area of lighter rainfall, and a corrugated appearance where vorticity maxima, labelled V1 to V5 in Figure 3(a), occur along the front.

A well-defined distortion of the rain band can be seen in both the radar image and the simulation, where it is associated with vorticity maximum V5 (Figure 3(a)). A less well-defined distortion in the rain band can be seen just to the west of the town of Scunthorpe in the radar image, and in the simulation is associated with a vorticity maximum, V1. We shall examine this feature in detail in section 3.2 and address the origin of the near-surface wind-speed maximum associated with V1 in section 3.3.

The simulated rain band is oriented in a slightly more north-east–south-west direction compared with the radar observation. Where the simulated front interacts with the northern and southern boundaries of the highest resolution, nested grid there is some distortion of the frontal structure. Experiments with different grids (not shown) confirm that the computational solution was not affected beyond 5–10 grid points near the grid wall.
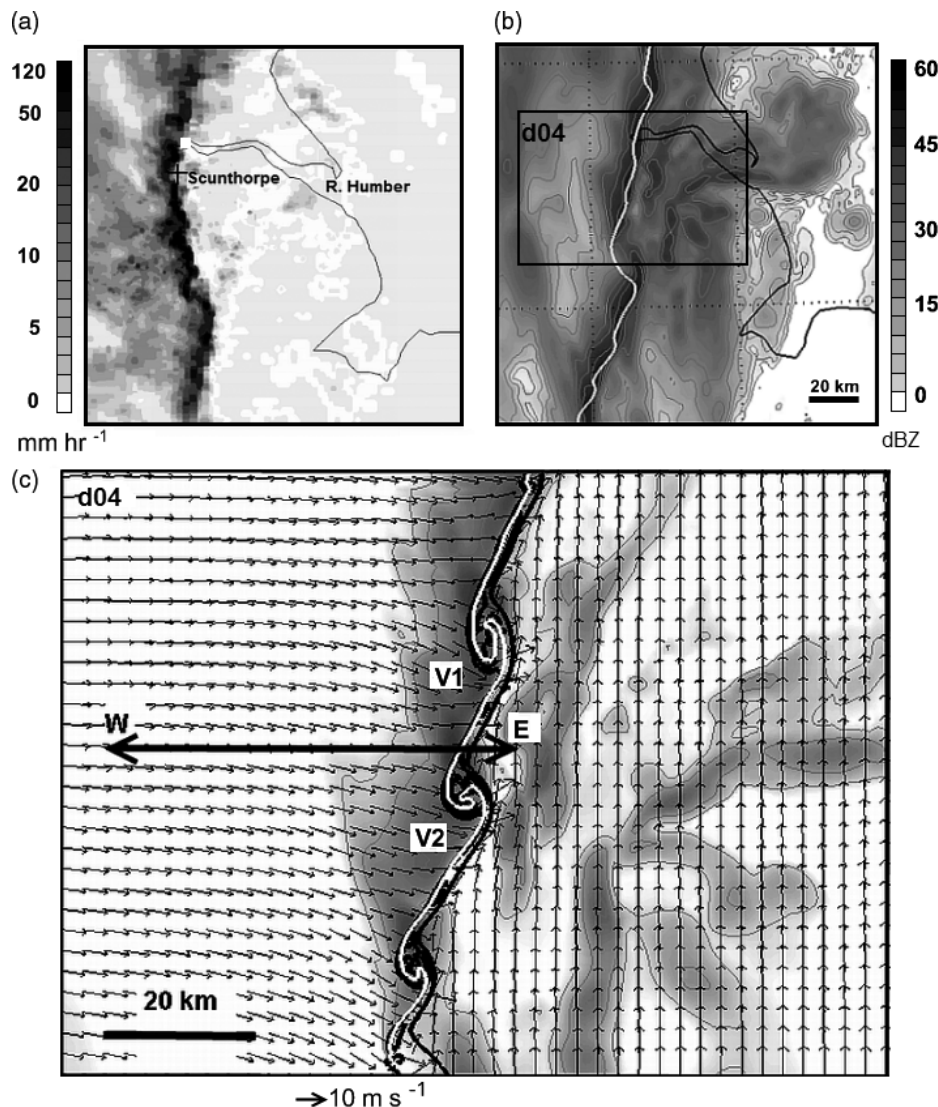

Figure 4. Comparison of high-resolution radar imagery with model fields. (a) UK network radar image at 0615 UTC (courtesy and copyright NetweatherUK and UKMO). The image has been post-processed and smoothed. Rain rate scale left-hand side. (b) Section of model domain d03 at 0550 UTC. Model simulated composite radar reflectivity field (dBZ), shaded, scale right-hand side, light grey contours every 5 dBZ. θ_e 314 K at 975 hPa: bold, white contour. The area of model domain d04 is outlined. (c) The whole of model domain d04, at 0550 UTC. Simulated composite reflectivity (dBZ), >35 dBZ, shaded and vertical vorticity (s^{-1}) at 925 hPa, bold contours >0.01 s^{-1}. Earth relative flow vectors every fourth grid point at 975 hPa. θ_e 314 K at 975 hPa: bold, white contour. Selected vorticity maxima V1, V2 are labelled. The line W–E shows the section of Figure 5.

Subjective assessment suggests that the model under-depicts the stratiform rainfall behind the front and over-depicts precipitation ahead of the front. No objective assessment of the quantative precipitation prediction performance of the model was undertaken, but these issues are not thought to affect the conclusions of the present study.

A 50 km long cross-section normal to and through the southern part of the bowing segment of the front at 0550 UTC is shown in Figure 5. The leading edge of the SCF is characterized by intense vertical ascent, up to $\sim$7.5 m s^{-1}. Pre-frontal air flows up and then slantwise and rearward over a shallow, intruding nose of cold air, defined by the 314 K θ_e contour. This lower-θ_e air has a system (front) relative velocity of $\sim$10 m s^{-1} at $\sim$750 m height some 30 km behind the front. The axis of this 'rear inflow' jet is indicated in Figure 5. Similar rear inflow jets have been observed and simulated in other studies for both NCFRs and mesoscale convective systems (MCS) (Smull and Houze, 1987; Browning *et al.*, 1997). The intruding lower-θ_e air mass appears to have gravity-current-like characteristics (Simpson, 1997), consisting of cold, relatively shallow and dense air with wave-like perturbations along its top at $\sim$1.5 km height and a raised frontal head that overrides a shallow layer of warmer air at the surface. Again, these features have been observed and characterized in previous studies (Carbone, 1982; Browning *et al.*, 1997). Just behind the immediate area of ascent at the front there is precipitation falling into the head of the intruding colder air mass, and here isopleths of θ_e descend towards the ground.

In summary, the simulated cold front bears a strong resemblance to the limited radar imagery available and possesses many features previously described for rain bands of this type:

- intense ascent and precipitation at the leading edge of the SCF – 'line convection';
- a sharp gradient in air-mass characteristics as defined by θ_e;
- a strong pre-frontal low-level jet;
- a weakly unstable pre-frontal environment;
- a gravity-current-like post-frontal airmass with a rear inflow jet.

3.2. Structure and evolution of a misocyclone

In this section we examine in detail the morphology and evolution of misocyclone V1 and a region of strong straight-line winds that forms along its southern flank.

In order to analyse the evolution of this feature, plots are presented in Figure 6 of the evolution of near-surface vertical vorticity, vertical velocity and horizontal wind-speed fields centred on the evolving vorticity maximum. Vertical and horizontal sections through the feature at the time of peak vertical vorticity (0530 UTC) are presented in Figure 7. Figure 7(a) shows the wind field relative to the vorticity maximum and the associated vertical velocity field. Figure 7(b) shows the vertical vorticity and vertical velocity fields along a north–south cross-section through the centre of the vortex.

Initially, the vertical vorticity field associated with the front has a two-dimensional sheet-like character and has a maximum located on the 'brow' of the frontal head at 1–1.5 km height (not shown). As the system evolves, the vertical vorticity field rolls up, intensifies and descends towards the surface. There is some evidence (not shown)
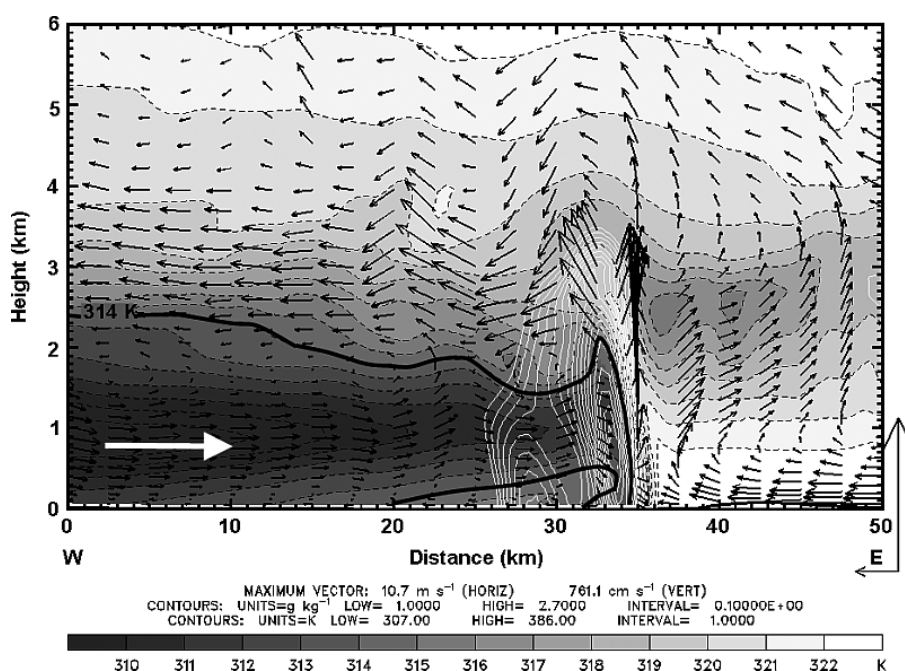

Figure 5. Cross-section through the simulated front along the line W–E in Figure 4(c) at 0550 UTC. Flow vectors, relative to the front, in the plane of the cross-section (m s^{-1}). θ_e (K), shaded and dashed contours every 1 K, scale at bottom, 314 K contour in bold. Rain mixing ratio (g kg^{-1}) at 0.1 g kg^{-1} intervals from 1.0 g kg^{-1} to 2.7 g kg^{-1}, white contours. The axis of the rear inflow jet (see text) is indicated schematically by the bold white arrow.
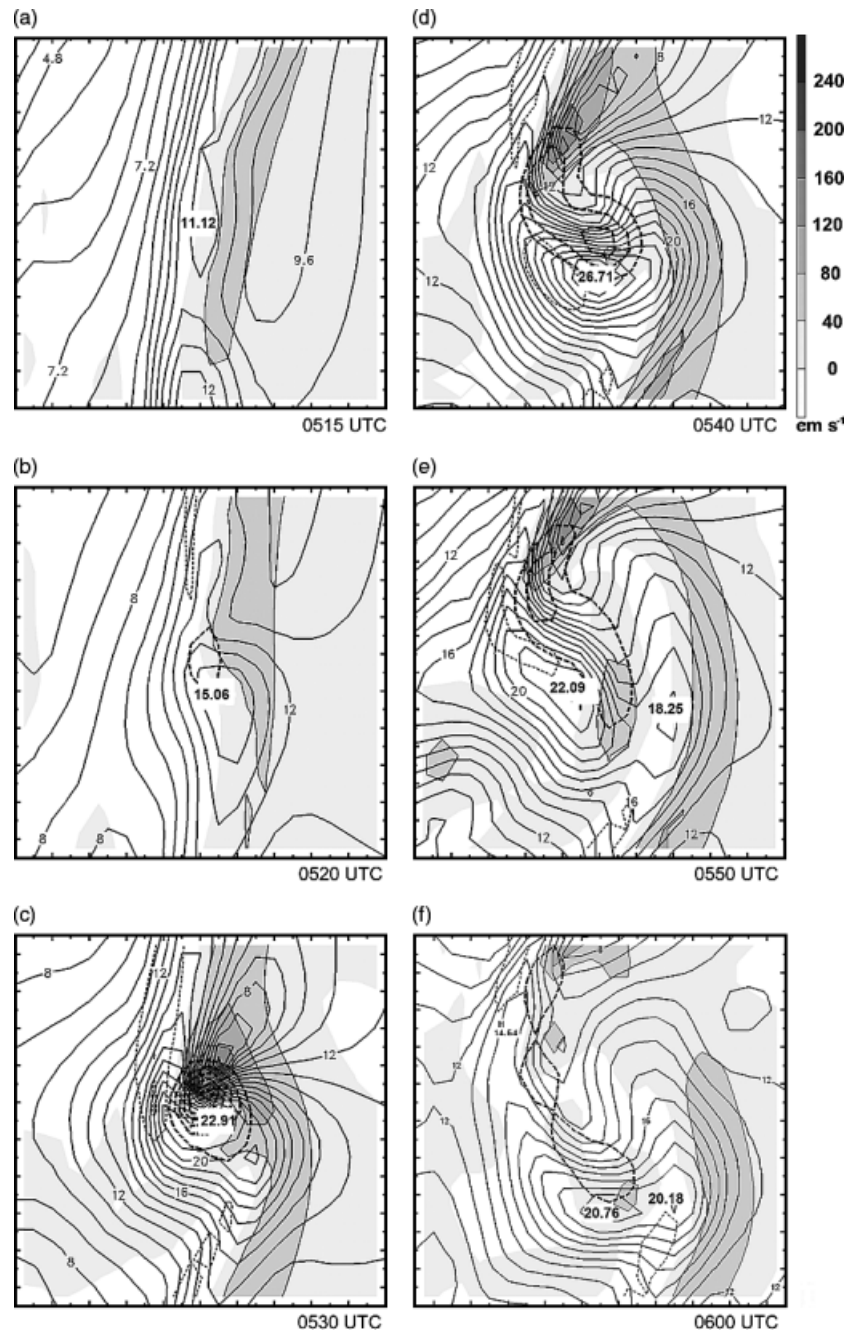
Figure 6. Plan views of the evolution of misocyclone V1 and wind-speed maximum. (a)–(f): horizontal sections (10×10 km) at 50 m above the surface, centred on misocyclone V1 at 0515 UTC then every ten minutes from 0520 UTC to 0600 UTC. Vertical velocity (cm s^{-1}), shaded, right-hand-side scale. Vertical vorticity, bold, dashed contours every 0.005 s^{-1} starting at 0.01 s^{-1}. Horizontal wind speed (m s^{-1}) contoured every 1 m s^{-1}. Local wind-speed maxima are annotated in bold. Tick marks every grid point (500 m).

for vortex merger and 'up-scale' growth of the vortices as previously reported in the idealized simulations of Lee and Wilhelmson (1997a) and observed by Marquis *et al.* (2007). Figure 6 shows that the vorticity maximum evolves from a perturbation or inflection point that develops along the front around 0515 UTC, with a closed 0.005 s^{-1} vertical vorticity contour at 0520 UTC (Figure 6(b)). The near-surface vertical vorticity increases steadily from ~0500 UTC, more rapidly after 0515 UTC and reaches a peak of 0.04 s^{-1} at 0530 UTC before declining rapidly (shown later in Figure 9(a)). By 0530 UTC there is a discrete, coherent vertical vorticity

maximum, approximately 2 km in diameter, with a closed circulation and immediately to the north and east a vertical velocity maximum. The structure of the misocyclone at this time is depicted in Figure 7. The low-level vorticity maximum is tilted towards the north beneath a similarly tilted interface between strong ascent and descent.

By 0540 UTC the vorticity maximum loses its coherence, becoming double-centred and then elongated (Figure 6(d)). The wind speed on the southern flank of the developing misocyclone increases to reach a peak of 27.7 m s^{-1} at 0542 UTC (see Figure 8(a)) and then declines. A further, but less intense, wind-speed
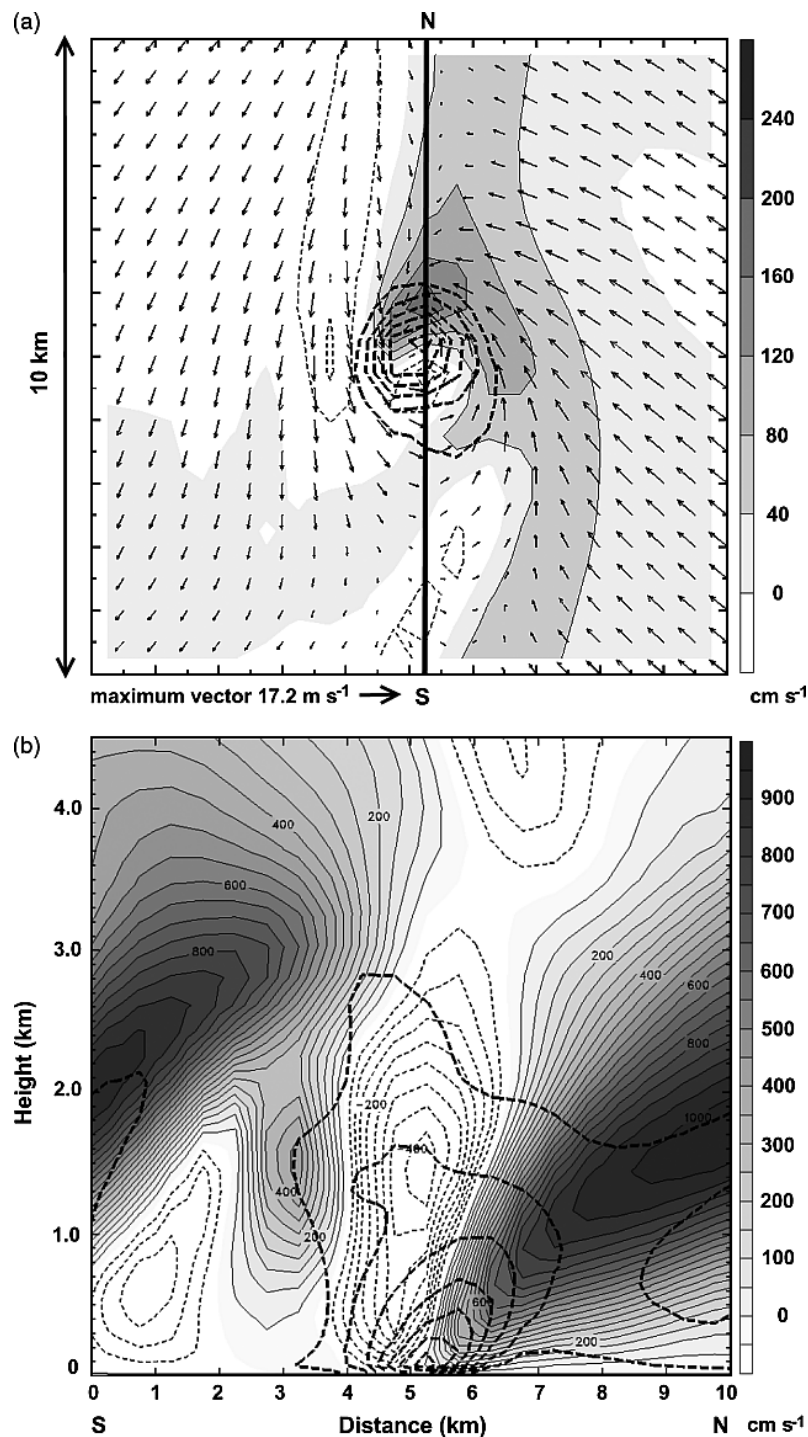
Figure 7. Horizontal and vertical sections through misocyclone V1 at 0530 UTC corresponding to the time of peak vertical vorticity. (a) Flow vectors at 50 m above the surface relative to the vorticity maximum (m s^{-1}); vertical vorticity, bold, dashed contours every 0.005 s^{-1} starting at 0.01 s^{-1}, light dashed contours where negative; vertical velocity (cm s^{-1}), shaded. Tick marks every grid point (500 m). The location of the vertical cross-section is labelled N–S.(b) Vertical cross-section along the line N–S in Figure 7(a). Vertical vorticity, bold, dashed contours every 0.005 s^{-1} starting at 0.01 s^{-1}; vertical velocity (cm s^{-1}), shaded and light contours, dashed where negative.

maximum develops where the SCF bows forward. A clear gap structure develops in the vertical velocity field (Figure 6(f)), as the southern segment of the front bows forward. This evolution in structure strongly resembles observations of radar reflectivity imagery, notably the 'broken-S' pattern, from cold-season NCFRs in the United States (McAvoy *et al.*, 2000; Grumm and Glazewski, 2004; Lane and Moore, 2006).

3.3. Origin of the strongest wind gusts near the surface

In order to determine the origin of the air parcels with highest wind speed, an ensemble of back-trajectory histories relative to the system vorticity maximum were computed at 0542 UTC and a starting height of 50 m. Trajectory positions were computed every minute back to 0522 UTC. Results for an array of 16 × 12 trajectories
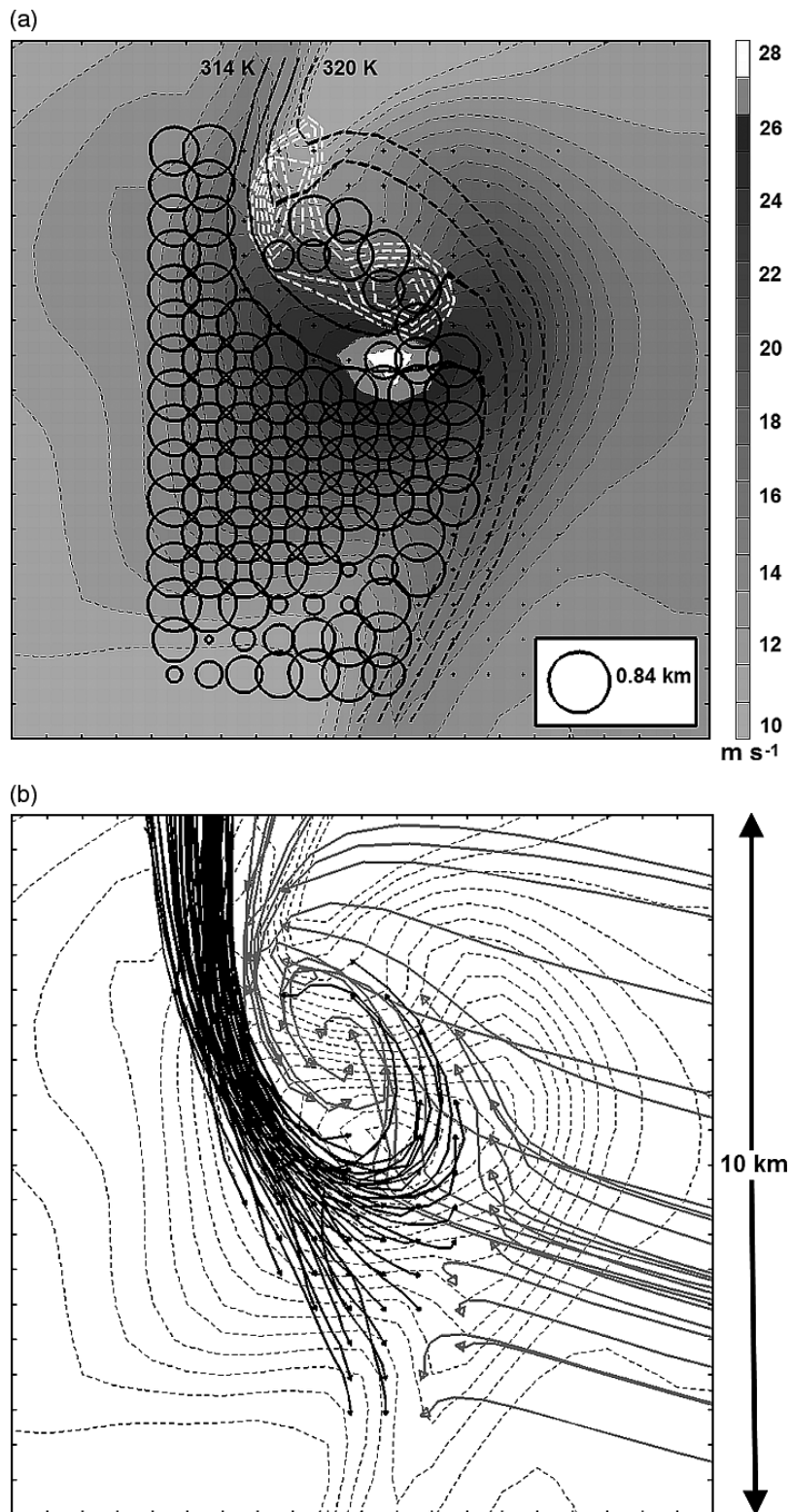
Figure 8. The histories of system-relative air parcel trajectories terminating in the misocyclone and near-surface wind-speed maximum. (a) Descent of back trajectories from 0542 to 0522 UTC for an array of 16×12 parcels terminating 50 m above the model terrain and centred on the misocyclone and wind-speed maximum. The diameter of the circles is proportional to the magnitude of the parcel descent (scale, inset). The 'dots' are circles for trajectories that have undergone descent of <100 m. Horizontal wind speed at 0542 UTC, light dashed contours and shaded every 1 m s^{-1}. θ_e: bold, black, dashed contours at 2 K intervals from 314–320 K. Vertical relative vorticity (s^{-1}): white dashed contours every 0.005 s^{-1} from 0.001 s^{-1}. (b) Time history of selected trajectories as before. Black trajectories are of air parcels with initial $\theta_e < 314$ K. Grey trajectories are of air parcels with initial θ_e of 322 K. Horizontal wind speed, light dashed contours at 1 m s^{-1} intervals. Tic marks every grid point (500 m).

are shown in Figure 8(a). Here, the widths of the circles centred on the starting position of the back trajectory are proportional to the degree of descent the parcel has experienced. A subset of system-relative trajectories is plotted in Figure 8(b) showing their time history. It can be seen that most of the parcels that undergo the greatest descent, up to 800 m, are located on the cold side of the frontal boundary, here demarcated by the 314–320 K θ_e contours. Analysis of tabulated trajectory properties (not shown) suggests that the strongest descent occurs just before or at 0530 UTC on the rear flank of the misocyclone, when the vorticity pattern has maximum coherence. Further parcels in the centre of the misocyclone also undergo strong descent. Air parcels that originate with θ_e of ~314 K do so on the north-western flank of the misocyclone with a starting height of 300–840 m. Air parcels that originate with a θ_e of ~322 K do so on the warm side of the front at low levels (<100 m). Although most of the parcels with the highest wind speeds, >25 m s^{-1}, originate in the cold air, a few also have high starting θ_e, and originate to the south-east of the system.

In summary, although it is likely the model does not fully resolve the region of most intense winds, Figure 8(a) and 8(b) demonstrate that air parcels associated with the highest near-surface winds along the bowing segment of the front and in the wind-speed maximum mostly originate in the high-momentum air associated with the rear inflow jet discussed in section 3.1. The misocyclone circulation appears to enhance the advection of these air parcels down to low levels. Relatively few of the parcels attaining high near-surface wind speeds originate in the high θ_e pre-frontal airmass.

3.4.   Properties of five misocyclones

Further simulations were conducted in which domain d04 was moved to the south-west of its position in the simulation presented above. All other aspects of the model configuration remained the same. This enabled us to examine a greater length of the front at very high resolution. In total we were able to identify five misocyclones (labelled V1–V5 in Figure 3(a) according to their selection from the domains), undistorted by interaction of the front with the walls of the computational domains.

The mean diameter of the five misocyclones, as defined by the 0.015 s^{-1} vertical vorticity contour, was found to be 1.38 km (range 1.07–1.55 km) at 50 m above the surface. The mean CAPE value, estimated immediately to the north-east of the misocyclone centre, where the CAPE was largest, was found to be only 158 J kg^{-1} (range 80–205 J kg^{-1}). No correlation was found between the CAPE of the misocyclone environment and circulation intensity, unlike Lee and Wilhelmson (1997b). The estimated width of the shear zone was 2–3 km. Multiplying a value of 2.5 km for the shear zone width by a factor of 7.5 gives 18.75 km for the distance between vortices expected by theory, if the disturbances were due to HSI (Miles and Howard, 1964). This is in good agreement with the mean

separation between vortex centres of 18.2 km (range 17.4–19.4 km) from the model (not shown).

Plots of the temporal evolution of vertical vorticity, vertical velocity and near-surface wind speed on the flanks of the misocyclone are shown in Figure 9, where the properties of the misocyclones are plotted with respect to the time of maximum vertical vorticity for each circulation. All of the misocyclones have rather similar time histories of vertical vorticity and the misocyclone we examine in detail, V1, seems typical in this respect. However its wind-speed maximum, occurring some 12 minutes after the time of peak vertical vorticity, exceeds all the others in intensity. We attribute this time difference, and a similar time difference for V2, to the time taken for the descent of air parcels from the level of the rear inflow jet. The reason why these two misocyclones, but not others, develop distinct near-surface wind-speed maxima is not clear from our simulations. Only for V1 and V5 does the time of maximum vertical velocity correspond to the time of maximum vertical vorticity. Finally, the reason why vertical velocity and vertical vorticity corresponded strongly for some misocyclones, but not others, is again unclear.

4.   Discussion

In summary, we found that our simulation produced a rain band that strongly resembled an intense cold front seen in radar imagery and had characteristics typical of previously observed and simulated NCFRs, most notably a gravity-current-like structure fed by a rear inflow jet. The resulting line convection had perturbations along its length that evolved into gap structures collocated with vertical vorticity maxima having small closed circulations, i.e. misocyclones. South of the misocyclones and the gaps the rain band bowed forward. The distance between vorticity maxima was consistent with theory for HSI. These results are consistent with recent modelling and observational studies of NCFRs (e.g. Jorgensen *et al.*, 2003; Wakimoto and Bosart, 2000).

Using a high-resolution grid, we examined the evolution of one misocyclone in detail. Figure 7 shows that the tilted vorticity maximum is collocated near the surface with a tilted interface between strong vertical ascent and descent. Vortex stretching and hence brief tornadogenesis is possible in a small region on the northern flank of the vortex, although none of the damage actually reported on this occasion was unambiguously attributed to tornadoes. At this time (0530 UTC) there is a shallow (~200 m) layer of negative static stability at the surface in this region (not shown), which may contribute to tornadogenesis. However, convergence into updraughts due to other causes, such as the main cold-frontal density current head or the dynamics of the misocyclone vortex, would be the major contribution to vortex stretching for any incipient tornado forming in the frontal shear zone. Any tornado circulation would likely be short-lived and weak, and cannot be resolved by the model at this grid spacing. Tornadogenesis associated with misocyclones in the presence
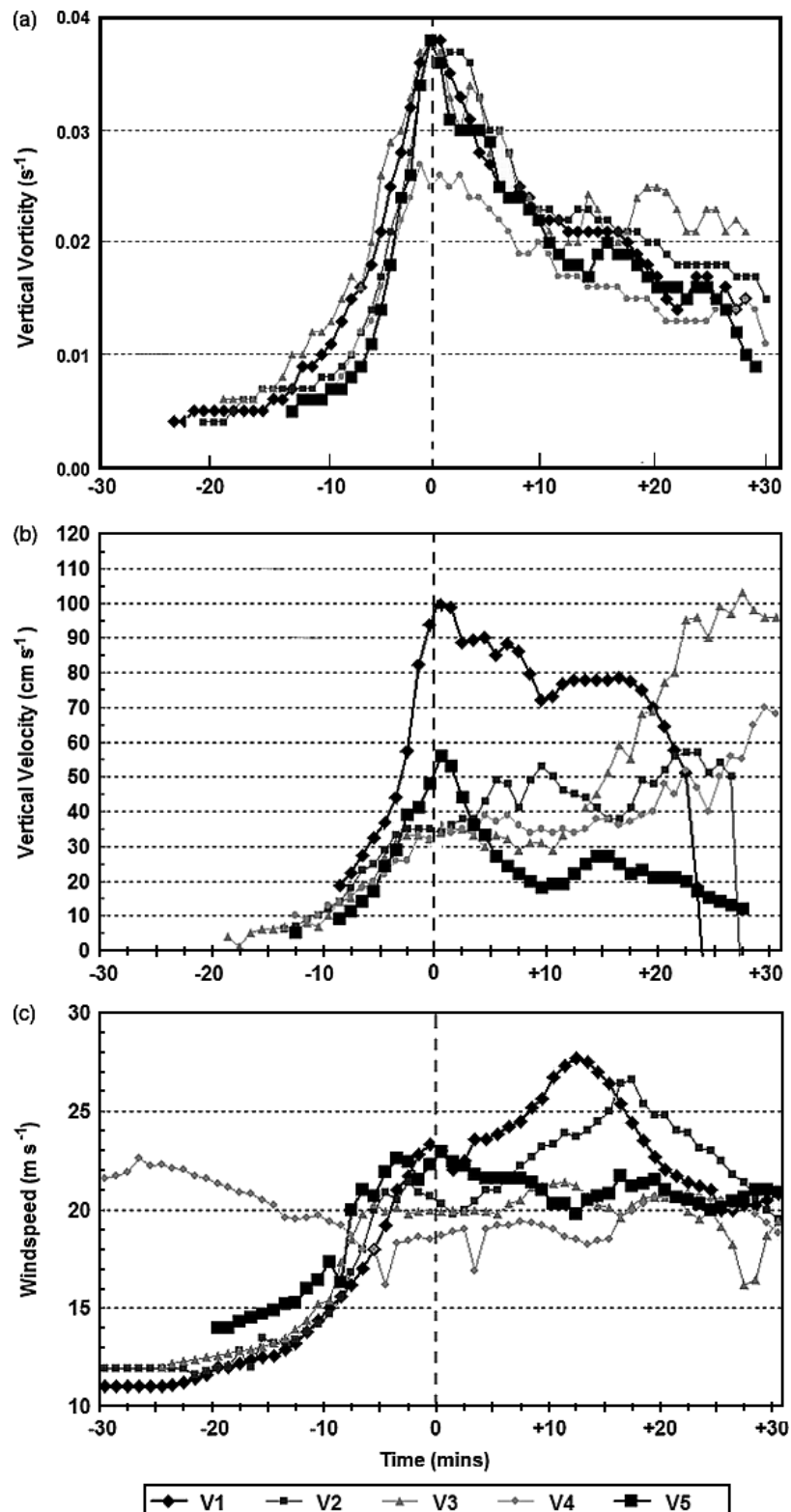
Figure 9. Properties of misocyclones V1–V5. (a) Vertical vorticity (s^{-1}) at 50 m above the surface. (b) Vertical velocity (cm s^{-1}) at 50 m above the surface. (c) Associated maximum horizontal wind speed (m s^{-1}) at 50 m above the surface. Each plot has been centred on the time of maximum vertical vorticity for each misocyclone (the '0 minutes' datum).

of HSI has previously been observed (Carbone, 1982, 1983) and simulated under idealized conditions (Lee and Wilhelmson, 1997b).

A key result of the present study is that we found a strong (straight-line) near-surface wind maximum on the southern flank of each misocyclone. This region of strong winds occurred after the misocyclone circulation attained peak vertical vorticity and was due to the combined translational and rotational motion of the misocyclone, which accelerated relatively cold, high-momentum air

that was descending towards the SCF. This air originated in the rear inflow jet. The presence of a very shallow layer of weak convective instability where low-θ_e air overrides warmer air at the surface may contribute to the formation of strong surface wind gusts.

These results for an NCFR in a weakly unstable environment are similar to the results of Trapp and Weisman (2003) for QLCSs in highly unstable environments. Their idealized simulations indicated that the strongest, most damaging straight-line winds occurred on the flanks of evolving mesocyclones. Intense wind-speed maxima produced by the downward transport of momentum on the flanks of meso- to miso-scale vortices appear to be a feature common in many severe convective systems, including supercell storms and bow echo squall lines (Wakimoto, 2001, section 7.4). Recently Wheatley and Trapp (2008) have reported the results of 'real-data' simulations of a tornadic cool-season QLCS in the continental United States and attributed the formation of mesovortices to HSI. Our results, also obtained in a non-idealized modelling setting, extend the prevalence of this phenomenon to the regime of strongly forced systems in weakly unstable environments in the 'maritime' environment of the United Kingdom.

Trapp *et al.* (1999), McAvoy *et al.* (2000) and Lane and Moore (2006) have drawn attention to the challenges posed to operational meteorologists by tornadoes and straight-line winds along QLCSs and NCFRs. Forecasting and nowcasting of such phenomena is a test of the limits of current modelling and operational radar capabilities.

5. Conclusions and further research

We have conducted high-resolution numerical simulations of an intense cold front, which produced damaging winds across the UK. The model initial and boundary conditions were supplied by data from an operational global model. The results of the simulations compare favourably with available radar imagery and conform to previous observations, simulations and conceptual models of NCFRs. The simulated front has a strong morphological resemblance to a gravity current of cold, dense air fed by a rear inflow jet. The formation of vortical circulations – 'misocyclones' – along the leading edge of the front has been shown to be consistent with the theory for HSI. The early stages of the misocyclone life cycle were found to be briefly favourable for vortex stretching and possible formation of a tornado parent circulation, which cannot be resolved by the model. We found that the formation of the misocyclones was accompanied by the development of long, narrow (length:width > 10:1) swathes of strong (>25 m s^{-1}) near-surface horizontal wind speeds. Trajectory analysis of air parcels terminating in the region of one such misocyclone showed that the majority of them originated in the cold air of the rear inflow jet and descended along the flanks of the vortex.

We have two possible explanations for the reported localized damage occurrences in the present case: (1) a narrow zone of straight-line winds on the southern flank of the misocyclone as the gap structure develops and (2) a brief, weak tornado on the northern flank of the misocyclone in the early stages as the frontal inflection point develops. It is not clear that reports of damage in this case can be attributed solely to either tornadoes or straight-line winds. When investigating and reporting damaging events along NCFRs, more care needs to be taken to differentiate between tornadic and straight-line wind damage. Future research should combine radar observations (ideally Doppler radar), modelling and field study of damage tracks.

Further simulations at higher resolution are planned in order to better resolve the vorticity and wind-speed maxima. Further studies are required to understand the generality and applicability of our results and the utility of high-resolution operational NWP models in predicting the timing and location of damaging wind phenomena on ana-cold fronts in particular, and low CAPE/high shear mesoscale systems in general.

References

Bradbury WMS, Deaves DM. 1994. The dependence of gust factor probabilities on convective activity: analysis conducted for Eurotunnel. *Meteorol. Appl.* **1**: 159–164.

Bradbury WMS, Deaves DM, Hunt JCR, Kershaw R, Nakamura K, Hardman ME, Bearman PW. 1994. The importance of convective gusts. *Meteorol. Appl.* **1**: 365–378.

Browning KA, Harrold TW. 1970. Air motion and precipitation growth at a cold front. *Q. J. R. Meteorol. Soc.* **96**: 369–389.

Browning KA, Roberts NM. 1996. Variation of frontal precipitation structure along a cold front. *Q. J. R. Meteorol. Soc.* **122**: 1845–1872.

Browning KA, Roberts NM, Illingworth AJ. 1997. Mesoscale analysis of the activation of a cold front during cyclogenesis. *Q. J. R. Meteorol. Soc.* **123**: 2349–2375.

Carbone RE. 1982. A severe frontal rainband, Part I: Stormwide hydrodynamic structure. *J. Atmos. Sci.* **39**: 258–279.

Carbone RE. 1983. A severe frontal rainband. Part II: Tornado parent vortex circulation. *J. Atmos. Sci.* **40**: 2639–2654.

Chen F, Dudhia J. 2001. Coupling an advanced land-surface/hydrology model with the Penn State/NCAR MM5 modeling system. Part I: Model description and implementation. *Mon. Weather Rev.* **129**: 569–585.

Dudhia J. 1989. Numerical study of convection observed during the Winter Monsoon Experiment using a mesoscale two-dimensional model. *J. Atmos. Sci.* **46**: 3077–3107.

Fujita TT. 1981. Tornadoes and downbursts in the context of generalized planetary scales. *J. Atmos. Sci.* **38**: 1511–1534.

Grumm RH, Glazewski M. 2004. Thunderstorm types associated with the 'broken-S' radar signature. Preprints, *22nd Conf. on Severe Local Storms*, 4–8 October 2004, Myannis, MA. American Meteorological Society: MA, USA. CD-ROM: P7.1.

Haurwitz B. 1949. The instability of wind discontinuities and shear zones in planetary atmospheres. *J. Meteorol.* **6**: 200–206.

Hobbs PV, Biswas KR. 1979. The cellular structure of narrow cold-frontal rainbands. *Q. J. R. Meteorol. Soc.* **105**: 723–727.

Hobbs PV, Persson P. 1982. The mesoscale and microscale structure and organization of clouds and precipitation in midlatitude cyclones. Part V: The substructure of narrow cold-frontal rainbands. *J. Atmos. Sci.* **39**: 280–295.

Houze RA Jr, Hobbs PV, Biswas KR, Davis WM. 1976. Mesoscale rainbands in extratropical cyclones. *Mon. Weather Rev.* **105**: 868–878.

James PK, Browning KA. 1979. Mesoscale structure of line convection at surface cold fronts. *Q. J. R. Meteorol. Soc.* **105**: 371–382.

Jorgensen DP, Pu Z, Persson P, Tao W-K. 2003. Variations associated with cores and gaps of a Pacific narrow cold frontal rainband. *Mon. Weather Rev.* **131**: 2705–2729.

Kain JS. 2004. The Kain–Fritsch convective parameterization: An update. *J. Appl. Meteorol.* **43**: 170–181.

Kobayashi F, Sugawara Y, Imai M, Matsui M, Yoshida A, Tamura Y. 2007. Tornado generation in a narrow cold frontal rainband – Fujisawa tornado on April 20, 2006. *SOLA* **3**: 21–24. DOI: 10.2151/sola.2007-006.

Lane JD, Moore PD. 2006. Observations of a non-supercell tornadic thunderstorm from terminal Doppler weather radar. *Preprints, 23rd Conf. Severe Local Storms*, St. Louis, MO. American Meteorological Society: MA, USA. CD-ROM: P4.5.

Lee BD, Wilhelmson RB. 1997a. The numerical simulation of nonsupercell tornadogenesis. Part I: Initiation and evolution of pretornadic misocyclone circulations along a dry outflow boundary. *J. Atmos. Sci.* **54**: 32–60.

Lee BD, Wilhelmson RB. 1997b. The numerical simulation of nonsupercell tornadogenesis. Part II: Evolution of a family of tornadoes along a weak outflow boundary. *J. Atmos. Sci.* **54**: 2387–2415.

Lin Y-L, Rarley LD, Orville HD. 1983. Bulk parameterization of the snow field in a cloud model. *J. Appl. Meteorol.* **22**: 1065–1092.

McAvoy BP, Jones WA, Moore PD. 2000. Investigation of an unusual storm structure associated with weak to occasionally strong tornadoes over the eastern United States. *Preprints, 20th Conf. Severe Local Storms*, Orlando, FL. American Meteorological Society: MA, USA 182–185.

Marquis JM, Richardson YP, Wurman JM. 2007. Kinematic observations of misocyclones along boundaries during IHOP. *Mon. Weather Rev.* **135**: 1749–1768.

Matejka TJ, Houze RA Jr, Hobbs PV. 1980. Microphysics and dynamics of clouds associated with mesoscale rainbands in extratropical cyclones. *Q. J. R. Meteorol. Soc.* **106**: 29–56.

Miles JW, Howard LN. 1964. Note on heterogeneous shear flow. *J. Fluid Mech.* **20**: 331–336.

Mlawer EJ, Taubman SJ, Brown PD, Iacono MJ, Clough SA. 1997. Radiative transfer for inhomogeneous atmosphere: RRTM, a validated correlated-k model for the longwave. *J. Geophys. Res.* **102**(D14): 16663–16682.

Noh Y, Cheon WG, Hong S-Y, Raasch S. 2003. Improvement of the K-profile model for the planetary boundary layer based on large eddy simulation data. *Boundary-Layer Meteorol.* **107**: 401–427.

Nolen RH. 1959. A radar pattern associated with tornadoes. *Bull. Am. Meteorol. Soc.* **40**: 182–185.

Sansom HW. 1952. A study of cold fronts over the British Isles. *Q. J. R. Meteorol Soc.* **8**: 275–279.

Simpson JE. 1997. *Gravity Currents in the Environment and the Laboratory* (2nd edn). Cambridge University Press: Cambridge.

Skamarock WC, Klemp JB, Dudhia J, Gill DO, Barker DM, Wang W, Powers JG. 2005. A Description of the Advanced Research WRF Version 2. *NCAR technical note*, NCAR/TN-468+STR NCAR: Boulder, CO; 100 pp.

Smull BF, Houze RA Jr. 1987. Rear inflow in squall lines with trailing stratiform precipitation. *Mon. Weather Rev.* **115**: 2869–2889.

Trapp RJ, Weisman ML. 2003. Low-level mesovortices within squall lines and bow echoes: Part II. Their genesis and implications. *Mon. Weather Rev.* **131**: 2804–2823.

Trapp RJ, Mitchell ED, Tipton GA, Effertz DA, Watson AI, Andra DL, Magsig ML. 1999. Descending and non-descending tornadic vortex signatures detected by WSR-88Ds. *Weather Forecasting* **14**: 625–639.

Wakimoto RM. 2001. Convectively driven high wind events. Severe convective storms. *Meteorological Monographs* **50**: 255–298.

Wakimoto RM, Bosart BL. 2000. Airborne radar observations of a cold front during FASTEX. *Mon. Weather Rev.* **128**: 2447–2470.

Wheatley DM, Trapp RJ. 2008. The effect of mesoscale heterogeneity on the genesis of mesovortices within quasi-linear convective systems. *Mon. Weather Rev.* **136**: 4220–4241.